

# Overcoming barriers for high temperature alloys: oxidation and ductility

---

Frauke Hinrichs<sup>a</sup>, Georg Winkens<sup>a</sup>, Lena Katharina Kramer<sup>a</sup>, Daniel Schliephake<sup>a</sup>, Gabriely Falcão<sup>a</sup>,  
Mathias Christian Galetz<sup>b</sup>, Haruyuki Inui<sup>c,d</sup>, Alexander Kauffmann<sup>a,e,\*</sup> and Martin Heilmaier<sup>a</sup>

<sup>a</sup> Institute for Applied Materials (IAM-WK), Karlsruhe Institute of Technology (KIT), Engelbert-Arnold-Str. 4, 76131 Karlsruhe, Germany

<sup>b</sup> DECHEMA-Forschungsinstitut, High Temperature Materials, Theodor-Heuss-Allee 25, 60486 Frankfurt am Main, Germany

<sup>c</sup> Department of Materials Science and Engineering, Kyoto University, Sakyo-ku, Kyoto 606-8501, Japan

<sup>d</sup> Center for Elements Strategy Initiative for Structural Materials (ESISM), Kyoto University, Sakyo-ku, Kyoto 606-8501, Japan

<sup>e</sup> Karlsruhe Nano Micro Facility (KNMFi), Karlsruhe Institute of Technology (KIT), Hermann-von-Helmholtz-Platz 1, 76344 Eggenstein-Leopoldshafen, Germany

\* corresponding author

mail: alexander.kauffmann@kit.edu (A. Kauffmann)

phone: +49 721 608 42346

---

## Abstract

1 The replacement of state-of-the-art Ni-based superalloys in high temperature applications to improve  
2 efficiency of energy conversion systems by novel metallic-intermetallic materials is currently obstructed  
3 by two major limitations of many candidate materials: a lack of oxidation resistance and/or a lack of  
4 ductility at low temperatures. No accurate predictive simulation capabilities for either of the two  
5 properties exist at the moment and, thus, the community still relies on disruptive observations.

6 The monolithic single-phase solid solution Cr-36.1Mo-3Si (at.%) presented in this article is prepared by  
7 a standard arc melting process. The crystal structure is disordered body centered cubic and the  
8 microstructure forms dendritic in the as cast condition. The alloy meets for the first time both  
9 fundamental requirements: (i) It exhibits resistance against pesting, nitridation and scale spallation as  
10 common problems of the oxidation of Cr and Mo based alloys at elevated temperatures up to 1100°C.  
11 (ii) At the same time, it shows sufficient ductility at low temperatures. The relevant mechanisms leading  
12 to that outstanding and yet unmet property combination are stressed based on a comparison to a Si free  
13 solid solution with the same Cr/Mo ratio and detailed microstructural investigations.

## Keywords

14 solid solution, oxidation resistance, ductility, single phase, deformation twinning

## 1. Introduction

15 Even with the rapid development of renewable energy sources, improving the efficiency of energy  
16 conversion from fossil or synthetic fuels remains a relevant problem. One striking example is that  
17 combustion engines in long-range aircrafts will not be replaced by all-electric technology within the  
18 upcoming decades [1,2]. Increasing operating temperatures is the most promising option to improve  
19 efficiency in this case, which requires replacing single crystalline Ni-based superalloys employed in the  
20 hottest sections of turbines by refractory element based metallic-intermetallic materials. The latter  
21 possess higher solidus temperatures beyond 2000°C, thus, they can withstand higher temperatures and  
22 stresses, potentially even without the need of additional cooling [3]. Promising examples for this are  
23 Mo-based alloys [4], Nb-based alloys [5], or refractory element-based complex concentrated alloys [6].  
24 While strength and creep resistance in these alloys are already superior to Ni-based superalloys,  
25 oxidation/corrosion resistance, mandatory to withstand the combustion atmosphere, and  
26 ductility/toughness, needed for failure tolerance and device setting, still display barriers for the  
27 development or application of candidate materials. Mo and most of its alloys suffer from catastrophic  
28 oxidation (“pestring”) above 500°C by the oxidation to MoO<sub>3</sub> along grain boundaries, which then  
29 evaporates due to its high vapor pressure [7]. The progress of oxidation leads to a quick disintegration  
30 of parts. In contrast, Cr is usually considered a passivating element that forms dense Cr<sub>2</sub>O<sub>3</sub> scales.  
31 However, Cr and Cr-based alloys suffer from scale spallation and nitridation when being exposed to air  
32 at high temperatures [8,9]. Any previous successful attempt to address oxidation resistance in these alloy  
33 systems came along with a significant deterioration in ductility as usually brittle intermetallic phases  
34 that provide passivating elements were needed in high amounts [10,11]. It is relevant to note here, that  
35 in general (i) Mo-based alloys are free of nitridation problems, (ii) Cr-based alloys do not exhibit pestring  
36 and (iii) disordered, body-centered cubic (bcc) solid solutions can possess ductility even at room  
37 temperature [12].

38 The protective effect of a Cr<sub>2</sub>O<sub>3</sub> layer formed on a Cr-Mo-Si alloy can depend decisively on the  
39 formation of a thin Si oxide sublayer at the interface between the outer Cr<sub>2</sub>O<sub>3</sub> scale and the metallic  
40 substrate as previously identified in Refs. [11,13]. These alloys were two-phase alloy with silicides and  
41 resistant against pestring and nitridation but brittle and eventually difficult to manufacture. Interestingly,  
42 the potentially ductile, disordered solid solution of the alloy in Ref. [11] also exhibited a continuous  
43 Cr<sub>2</sub>O<sub>3</sub> scale. In the present investigation, this (Cr,Mo,Si) solid solution was manufactured in monolithic  
44 condition to investigate whether a silicide phase is really needed to obtain oxidation resistance and if  
45 the solid solution is ductile.

46 To the best of our knowledge, the Si containing Cr-Mo solid solution derived from Ref. [11] and  
47 presented in this article meets for the first time both fundamental requirements regarding resistance  
48 against pestring, nitridation and scale spallation at elevated temperatures up to 1100°C as well as  
49 regarding sufficient ductility at low temperatures. The relevant mechanisms leading to that outstanding  
50 and yet unmet property combination are stressed based on a comparison to a Si free solid solution with  
51 the same Cr/Mo ratio and detailed microstructural investigations.

## 2. Constitution and Microstructure

52 The two alloys, Cr-37.2Mo (at.% are used throughout the article unless stated otherwise) and Cr-  
53 36.1Mo-3Si, were investigated in the as cast condition after arc melting (see Materials and Methods  
54 section for detailed description). The desired composition of the Si containing solid solution corresponds  
55 to the experimentally assessed one from Ref. [11] and both solid solutions possess the same Cr/Mo ratio  
56 for comparison purpose.

57 In Figure 1, scanning electron microscopy backscattered electron contrast (SEM-BSE) images of the  
58 coarse-grained, dendritic as cast microstructure are depicted for a) Cr-37.2Mo and b) Cr-36.1Mo-3Si.  
59 For both alloys, the SEM-BSE micrographs show a continuous transition in atomic number  $Z$  contrast  
60 between the dendrite core and the interdendritic regions. Chemical compositions were confirmed by  
61 SEM based energy dispersive X-ray spectroscopy (SEM-EDS) analysis and deviations from the average  
62 due to the dendritic microstructures are listed in Table 1. The minimum Cr/Mo ratio obtained is 1.30 to  
63 1.51 in the dendrite centers. The maximum Cr/Mo ratio in the interdendritic regions amounts to 2.05 to  
64 2.13. Si exhibits significant enrichment in the interdendritic regions of the Si containing solid solution.  
65 No secondary phases are present. The dendrite spacings were directly measured from secondary dendrite  
66 arms in SEM-BSE micrographs and averaged which yields  $(30 \pm 10) \mu\text{m}$  for Cr-37.2Mo and  $(52 \pm$   
67  $14) \mu\text{m}$  for Cr-36.1Mo-3Si. Interstitial contamination was determined using hot carrier gas extraction  
68 (HCGE). For both alloys, N and O are about 450 and 750 at.-ppm (95 and 170 wt.ppm), respectively.  
69 The contamination levels are low and representative for the arc melting method.

70 For the desired compositions, the liquidus  $T_L$  and solidus temperatures  $T_S$  were calculated using  
71 CALPHAD line simulations for equilibrium conditions. The determined temperatures are listed in  
72 Table 1. The solidification of Cr-37.2Mo initiates at  $2061^\circ\text{C}$  with a composition of Cr-54Mo for the first  
73 solid. This is higher than the experimentally detected composition of the dendrite cores due to off-centric  
74 analysis in the 2D sections and the extended probe size of SEM-EDS. Under equilibrium conditions  
75 solidification is completed at  $1941^\circ\text{C}$ . Due to non-equilibrium solidification in the arc melter,  
76 completion of solidification is retarded down to about  $1910^\circ\text{C}$  according to the experimentally  
77 determined composition of the interdendritic regions. In Cr-36.1Mo-3Si,  $T_L$  is reduced by 62 K and the  
78 composition of the first solid is Cr-52.6Mo-0.6Si according to the simulations. The experimentally  
79 obtained Mo enrichment of the dendrite cores is lower than the simulation results again. A similar trend  
80 is found for the Si depletion in the dendrite core. However, a qualitative agreement is obtained. The  
81 equilibrium solidification interval of the Si containing solid solution is calculated as  $\Delta T = 217 \text{ K}$  and is  
82 therefore larger than  $\Delta T = 120 \text{ K}$  of the binary alloy. The retardation of solidification by the fast cooling  
83 rate after arc melting might even reach  $1670^\circ\text{C}$  (solidus temperature of the experimentally determined  
84 composition of the interdendritic regions).

85 The crystal structures are identified by X-ray diffraction (XRD) as single-phase, body centered cubic  
86 (bcc) W prototype, Strukturbericht designation A2 (see the Supplementary Material S1). No secondary  
87 phases are found in agreement with the microstructural investigations. The cubic lattice parameters and  
88 crystallographic densities are determined as  $a = 3.003 \text{ \AA}$  and  $\rho = 8.42 \text{ g/cm}^3$  for Cr-37.2Mo and  
89  $a = 2.998 \text{ \AA}$  and  $\rho = 8.27 \text{ g/cm}^3$  for Cr-36.1Mo-3Si, respectively.

90 Compared to previously reported lattice parameters for similar solid solutions [14], no relevant  
91 deviations are detected. Si was previously noted to have no noticeable influence on the lattice parameter  
92 of these solid solutions [15,16].

93 In summary, the Si content marks the main difference between the two alloys discussed in this article.  
94 No distinct difference regarding the constituting phase, microstructure, Cr/Mo-ratio, density and lattice  
95 parameter are identified.

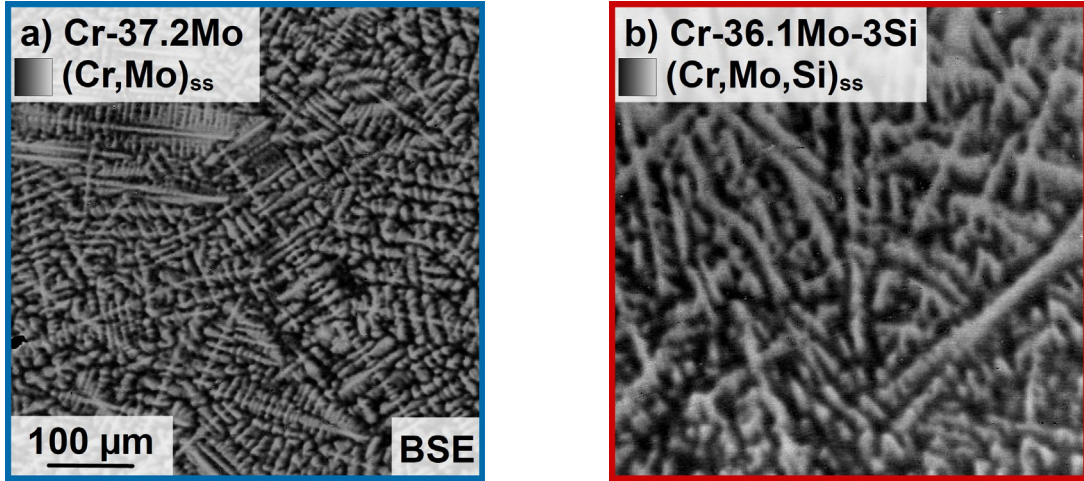


Figure 1: Dendritic, single-phase microstructure of the two alloys by SEM-BSE: (a) Cr-37.2Mo and (b) Cr-36.1-3Si.

Table 1: Confirmation of the desired alloy compositions, contamination levels and relevant physical properties, e.g. lattice parameters, densities, liquidus and solidus temperatures from SEM-EDS, HCGE and XRD analyses and thermodynamic calculations. “Rel. Cr/Mo” indicates the ratio of detected Cr and Mo contents.

		Cr-37.2Mo			Cr-36.1Mo-3Si		
		Total	Dendrite core	Inter-dendritic	Total	Dendrite core	Inter-dendritic
SEM-EDS	Cr / at.%	62.1	56.5	67.7	60.7	59.1	64.8
	Mo / at.%	37.9	43.5	32.3	36.6	39.0	31.6
	Si / at.%	–	–	–	2.7	1.9	3.6
	rel. Cr/Mo	1.63	1.30	2.13	1.63	1.51	2.05
HCGE	O / at.ppm	670 ± 340	–	–	770 ± 170	–	–
	N / at.ppm	460 ± 20	–	–	440 ± 10	–	–
XRD	$a / \text{Å}$	3.003	–	–	2.998	–	–
	$\rho / \text{g/cm}^3$	8.42	–	–	8.27	–	–
Simulation	$T_L / ^\circ\text{C}$	2061	–	–	1999	–	–
	$T_S / ^\circ\text{C}$	1941	–	–	1782	–	–
	$\Delta T / \text{K}$	120	–	–	217	–	–

### 3. Macroscopic Properties

#### 3.1 Oxidation

96 Since oxidation and peeling resistance are key requirements for novel high temperature refractory metal  
 97 alloys, Cr-37.2Mo and Cr-36.1Mo-3Si were tested in cyclic oxidation experiments. Cyclic oxidation  
 98 displays harsher conditions over isothermal oxidation due to superimposed thermal cycling, which will  
 99 reveal potential adherence problems of the formed oxide scales. Furthermore, it allows for acquiring  
 100 statistically relevant results as multiple samples are tested in parallel; this is of specific interest when  
 101 stochastic processes like spallation, buckling and evaporation occur during oxidation. In order to assess  
 102 potential peeling behavior, testing was performed at 800°C for up to 100 h. Oxidation experiments at  
 103 1100°C were conducted to investigate the possible application limits for those (chromia forming) alloys.  
 104 In Figure 2a, the area specific mass change is plotted against time for Cr-37.2Mo and Cr-36.1Mo-3Si  
 105 for oxidation at 800°C and 1100°C. The mean values and uncertainties (unless stated otherwise) from  
 106 at least three samples are depicted. Throughout the article “specific mass loss/change” always indicates  
 107 the *area* specific mass change.

108 For the Si free Cr-37.2Mo, continuous specific mass loss is recorded right from the first hour of oxidation  
109 at 800°C (continuous blue line in Figure 2a). After 100 h, the specific mass loss of the samples is  
110 between  $-5.5$  and  $-6$  mg/cm<sup>2</sup>. The specific mass loss of no more than  $-6$  mg/cm<sup>2</sup> is significantly smaller  
111 than for Mo-based alloys suffering from pesting. For the used sample geometry, pesting would result in  
112 specific mass loss of more than  $-100$  mg/cm<sup>2</sup> within the first hours of oxidation and complete  
113 disintegration of the material, like in high Si, multi-phase Mo-Si-Ti alloys in Ref. [17]. Similarly, the  
114 well-researched reference Mo-Si-B alloys with much higher amounts of Si of 9 to 12 at.% as compared  
115 to Cr-36.1Mo-3Si exhibit up to  $-50$  mg/cm<sup>2</sup> within the first hours of oxidation at 800°C [18]. Instead,  
116 the Cr-36.1Mo-3Si samples stay intact and a dark oxide scale is found after just one hour and loose,  
117 greenish, dust-like oxide(s) after prolonged oxidation up to 100 h. Further microstructural analysis of  
118 the oxide scales is provided in the latter parts of this article. The macroscopic sample geometry changes  
119 only marginally during the tests. However, the specific mass change indicates that the Si free alloy does  
120 not form a protective scale at 800°C and evaporation of volatile oxide still occurs.

121 At 1100°C, Cr-37.2Mo exhibits significant specific mass loss. In Figure 2a, the specific mass change of  
122 a single sample is depicted (as dashed blue line) instead of an average value of several samples as the  
123 onsets of rapid mass loss occurred erratically across all seven samples tested. Oxidation at 1100°C is,  
124 thus, considered beyond the capability limit of Cr-37.2Mo. Consequently, the oxide growth is not  
125 examined in detail any further.

126 For Cr-36.1Mo-3Si, reproducible specific mass changes are recorded at both, 800 and 1100°C. At  
127 800°C, the specific mass change (red continuous line in Figure 2a) is less than  $\pm 0.05$  mg/cm<sup>2</sup> after 100 h  
128 of oxidation and the uncertainty is smaller than the size of the symbols. Due to the small extent of mass  
129 change, no attempt was made to quantify the mass change kinetics. The oxidation mechanism is further  
130 assessed based on the scale growth kinetics in the latter stage of this article. The small mass change  
131 already indicates the absence of spallation and evaporation events and hints at a very good oxidation  
132 resistance at 800°C, unless specific mass loss through evaporation would exactly be counterbalanced by  
133 mass gain through scale formation. The samples exhibit a thin, translucent green oxide after the 1 h at  
134 800°C. After 100 h, a dark oxide scale has formed on the surface. Macroscopically, no spallation or  
135 disintegration of the material is observed. The sample geometry remains unchanged for 100 h of  
136 oxidation. The formation of a protective scale is confirmed by the scale analysis later in this article.

137 The Si containing Cr-36.1Mo-3Si shows a slightly discontinuous specific mass change at 1100°C with  
138 sequences of faster and slower oxidation (dashed red line in Figure 2a). This is indicative of a complex  
139 interplay between mass loss due to evaporation and mass gain due to scale growth by O ingress. After  
140 100 h, the specific mass change is  $-3$  to  $-4$  mg/cm<sup>2</sup>. While the sample geometry stays intact and no  
141 significant disintegration is observed, a dark gray oxide layer and several spots of green oxide(s) are  
142 found on the sample surface. There are regions on the surface, from which thin plate-like layers have  
143 detached.

144 Si addition is thus proven to exhibit an outstanding positive effect on the specific mass change at 800°C,  
145 which becomes barely detectable. Furthermore, it considerably improves the oxidation behavior at  
146 1100°C, as has been shown for Cr solid solutions with Si [8]. High volume fractions of silicide phases  
147 as commonly established in other Mo and Cr based alloys [4,8,19,20] are not necessary for a sufficient  
148 oxidation behavior. Instead, marginal amounts of silicide phases might be deliberately distributed to  
149 further improve mechanical strength and oxidation resistance without deterioration of ductility.

150 (Parabolic) oxidation rate constants based on the specific mass changes were not evaluated for the two  
151 alloys because the mass changes are either negative (superposition of evaporation and scale growth) or

152 too small for reasonable quantification of the rate law. Instead, the progression of scale growth is  
153 evaluated in Section 4.1 to study the oxidation mechanisms in more detail.

### 3.2 Mechanical Properties

154 Representative engineering stress-strain ( $\sigma_e - \varepsilon_e$ ) data are shown in Figure 2b for both compositions at  
155 room temperature and at 900°C. Deformation in the compression tests occurs serrated immediately from  
156 or shortly beyond the onset of plastic deformation for all test temperatures. The two alloys show  
157 extended plastic deformation of at least 6% and none of the samples fail before deliberately stopping  
158 the compression tests. The plastic strain detected in the setup was confirmed by measuring the heights  
159 of the specimens after testing. The number of identified stress drops during serrated flow remains  
160 approximately constant for both compositions across all temperatures with between 20 and 30 drops per  
161 sample tested up to the maximum plastic strains of > 6%. For all test temperatures up to 800°C, the  
162 stress drop magnitude is between 20 to 50 MPa while being significantly lower with only 10 MPa at  
163 900°C.

164 Whether plastic deformation is initiated by stress drops remains an open issue. Due to the discontinuities,  
165 the commonly used 0.2% offset yield strength was not used for strength assessment as the values are  
166 determined by the statistical appearance of individual stress drops. Instead, the stress at 1% plastic strain,  
167  $\sigma_{1\%}$ , was used for a more robust evaluation [21] and is presented in Figure 2c as a function of test  
168 temperature for both alloys. A large offset yield strength at room temperature of approximately  
169 1100 MPa is observed. Furthermore, strength decreases until a plateau of approximately 900 MPa is  
170 reached at 400°C (corresponding to  $0.30 \dots 0.33 T_S$ ), and is maintained for both alloys up to 700°C  
171 (corresponding to  $0.44 \dots 0.47 T_S$ ). Strength decreases beyond 700°C, where creep-controlled  
172 deformation occurs at the initial strain rate of  $1 \cdot 10^{-4} \text{ s}^{-1}$ . However, at 900°C (corresponding to  
173  $0.53 \dots 0.57 T_S$ ) still 760 MPa, equivalent to 70% of the room temperature strength, is observed. The  
174 detected strength values are mostly identical within the uncertainty ranges for both alloys, indicating no  
175 significant impact of Si on the strength of the alloys in the as cast condition.

176 To evaluate potential tensile ductility of the alloys, the engineering stress-strain data from Figure 2b are  
177 converted to true stress-true strain data  $\sigma_t - \varepsilon_t$  assuming volume conservation and prismatic sample  
178 shape. After smoothing the data, the true work hardening  $d\sigma_t/d\varepsilon_t$  is determined and compared to the  
179 Considère criterion  $\frac{d\sigma_t}{d\varepsilon_t} = \sigma_t$  [22], see Figure 2d. For all measurements, the true work hardening is larger  
180 than the true stress,  $\frac{d\sigma_t}{d\varepsilon_t} > \sigma_t$ . In case of extended plastic deformation, ductility in tensile tests can be  
181 limited by the localization of plastic deformation as a result of the geometrical-mechanical instability of  
182 the test. In order to achieve high ductility under tension, intrinsic work hardening must be larger than  
183 geometrical softening by the reduction of the cross-sectional area. This is constituted for the samples  
184 tested even at room temperature by  $\frac{d\sigma_t}{d\varepsilon_t} > \sigma_t$  for plastic strains below minimum 6%.

185 Unlike most silicide containing alloys, both solid solutions exhibit exceptional compressive ductility at  
186 room temperature in combination with a high strength level all the way up to 900°C. Even with the  
187 compression tests conducted in this study, a high work hardening beyond the Considère criterion is  
188 revealed as one of the fundamental prerequisites of tensile ductility.

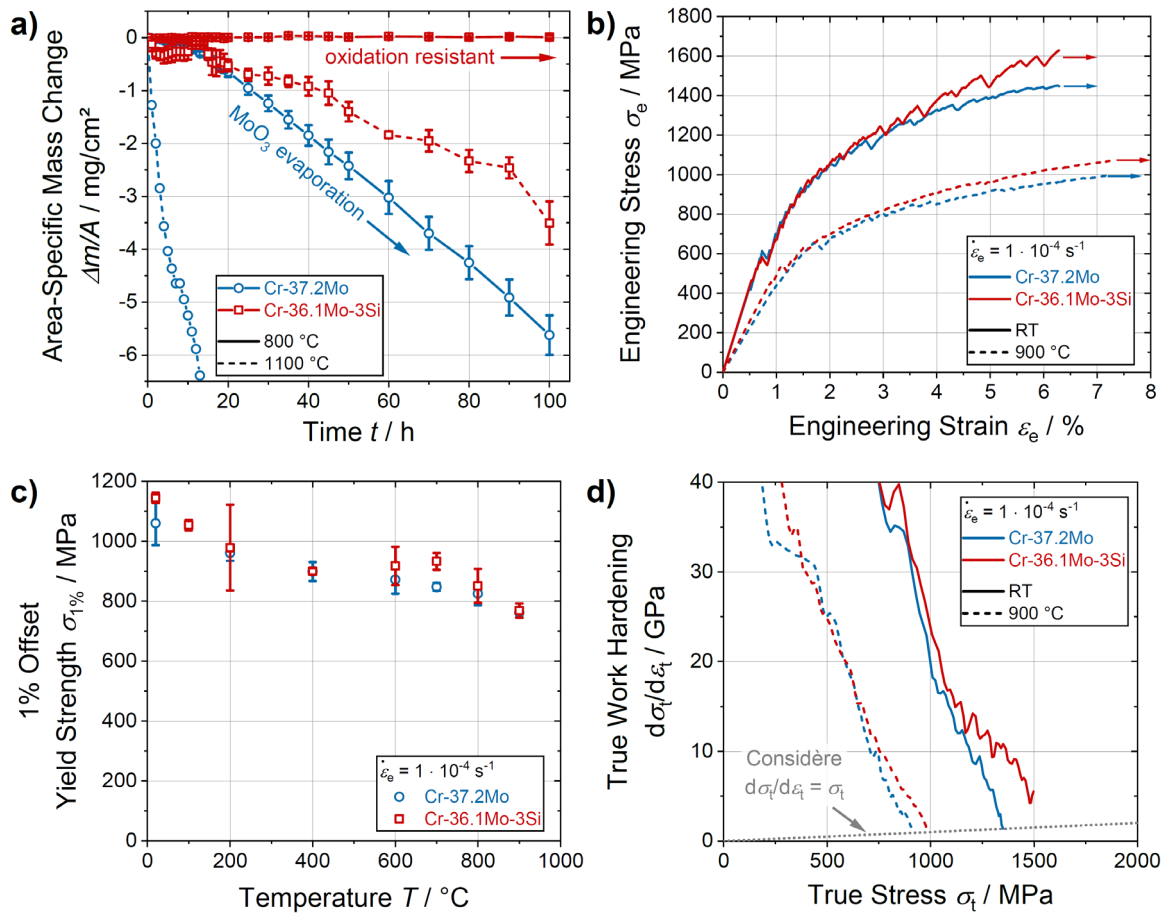


Figure 2: Macroscopic assessment of material properties of Cr-37.2Mo (blue) and Cr-36.1Mo-3Si (red): (a) Area-specific mass change during cyclic oxidation at 800°C, proving the superior oxidation behavior of Cr-36.1Mo-3Si. (b) Engineering stress-strain curves obtain from compression tests conducted at room temperature and 900°C, proving extended plastic deformation at all test temperatures. The tests were deliberately stopped before failure. (c) 1% offset yield strength as a function of temperature, proving high yield strength level even at 900°C. (d) True work hardening as a function of true stress extracted from the compression tests in (b), proving the capability against necking up to the plastic strains tested.

## 4. Microscopic Origins of the Materials Properties

### 4.1 Oxidation Mechanisms

189 The observed mass losses of Cr-37.2Mo already prove that no protective scales are formed at either  
 190 temperature tested on this alloy. At 800°C, the only crystal structure identified at the sample surface  
 191 after oxidation via XRD is a Corundum prototype (Strukturbericht designation D5<sub>1</sub>, see Supplementary  
 192 Material S2). In conjunction with SEM-EDS, the scale is identified as monolithic Cr<sub>2</sub>O<sub>3</sub> (see  
 193 Supplementary Material S3). The oxide scale is composed up of a porous, layered structure of Cr<sub>2</sub>O<sub>3</sub>  
 194 with a total thickness of  $(88 \pm 14) \mu\text{m}$  after 100 h. The scale growth occurs almost linear at  
 195 approximately  $(2.4 \pm 0.1) \cdot 10^{-8} \text{ cm/s}$  ( $R^2 \approx 0.99$ , see Supplementary Material S4) further proving that  
 196 no protective scale has formed. SEM-EDS analysis reveals that the interface between Cr<sub>2</sub>O<sub>3</sub> and the  
 197 substrate material is enriched in Mo due to Cr consumption by the oxidation to Cr<sub>2</sub>O<sub>3</sub>. Coarse Mo rich  
 198 regions at the interface are formed up to 15  $\mu\text{m}$  in thickness. The continuous mass loss of Cr-37.2Mo at  
 199 800°C (see Figure 2a) is attributed to MoO<sub>3</sub> evaporation. Significant evaporation of CrO<sub>3</sub> is not expected  
 200 below 900°C [23]. Failure of the non-protective Cr<sub>2</sub>O<sub>3</sub> leads to the rapid oxidation of the underlying Mo  
 201 enriched regions to MoO<sub>3</sub> and mass loss due to its evaporation. Another layer of Cr<sub>2</sub>O<sub>3</sub> is formed and  
 202 the accompanying O ingress compensates some of the mass loss by evaporation. The repeating sequence  
 203 of scale formation and evaporation leads to the porous, layered structure of the scale. As previously

204 mentioned, 1100°C scales on Cr-37.2Mo were not further investigated as this oxidation temperature is  
205 beyond the capability limit of that alloy.

206 For Cr-36.1Mo-3Si, SEM-EDS elemental maps of the scales after 100 h of cyclic oxidation at 800°C  
207 are displayed in Figure 3a. Figure 3b depicts a respective schematic scale mockup. The SEM-EDS maps  
208 show the formation of a continuous, well-adhered, crack-free Cr oxide layer of uniform thickness. XRD  
209 analysis confirms that the scale consists of Corundum prototype Cr<sub>2</sub>O<sub>3</sub> (D5<sub>1</sub>, see Supplementary  
210 Material S2). Continuous white lines in Figure 3a indicate this Cr<sub>2</sub>O<sub>3</sub> scale. Below the scale, a thin, Cr  
211 depleted and Mo enriched region is observed. Since the oxide scale is very thin, the Mo rich W prototype  
212 crystal structure below the Cr<sub>2</sub>O<sub>3</sub> scale is still detected via XRD. The lattice parameter of 3.125 Å  
213 corresponds to a Mo content of about (90 ± 2) at.% [14]. Neither in SEM-EDS nor XRD, nitride phases  
214 are identified. Hence, the Mo enrichment below the oxide scale acts as a barrier against nitridation as  
215 was found already for other Cr-Mo-Si alloys [11,24]. The addition of even small amounts of 3 at.% Si  
216 in the present alloy leads to a remarkable reduction of the scale thickness from about 90 μm to only  
217 (1.6 ± 0.5) μm after 100 h of cyclic oxidation. The scale growth follows a slow, cubic growth law at  
218 (1.1 ± 0.1) · 10<sup>-17</sup> cm<sup>3</sup>/s ( $R^2 \approx 0.97$ , see Supplementary Material S4) consistent with the previously  
219 discussed observations on the small mass change after 100 h. Even though SEM-EDS does not resolve  
220 a Si enrichment at the scale substrate interface, it can be assumed that a very thin and potentially  
221 discontinuous Si oxide layer forms as it has been identified by scanning transmission electron  
222 microscopy analysis in Ref. [11]. The relevant features in the schematic representation in Figure 3b are  
223 (i) the thin, continuous Cr<sub>2</sub>O<sub>3</sub>, (ii) the Mo enriched subsurface layer and (iii) the formation of Si oxide.

224 A beneficial influence of Mo on the oxidation resistance of Cr alloys has been observed before in entirely  
225 intermetallic Cr-30Mo-30Si consisting of a two-phase Cr<sub>3</sub>Si-Cr<sub>5</sub>Si<sub>3</sub> microstructure [24] and in the Mo  
226 lean, two-phase Cr-7Si-2Mo which consists of a (Cr,Mo,Si) solid solution matrix and (Cr,Mo)<sub>3</sub>Si  
227 precipitates [13]. For the intermetallic Cr-30Mo-30Si, excellent oxidation resistance up to 200 h in the  
228 entire temperature range from 500°C to 1100°C is found. Above 1100°C, however, increased specific  
229 mass loss is recorded. Up to 700°C, only Cr<sub>2</sub>O<sub>3</sub> is detected. Between 700°C and 1300°C, both Cr<sub>2</sub>O<sub>3</sub>  
230 and SiO<sub>2</sub> are identified. Above 1300°C, only SiO<sub>2</sub> is verified. From the results in Ref. [24], it was  
231 concluded that Mo addition to Cr-Si alloys promotes the formation of SiO<sub>2</sub> consistent with results from  
232 the present study. For Cr-7Si-2Mo, specific mass gains after 100 h at 1200°C are slightly reduced to  
233 +5.5 compared to +8 mg/cm<sup>2</sup> for a Mo free reference alloy with the composition Cr-9Si [13]. However,  
234 the scale thickness after 100 h being 15 to 22 μm is not significantly influenced by the Mo addition. A  
235 solid solution layer with an increased Mo content is observed underneath the Cr<sub>2</sub>O<sub>3</sub> top layer. The Mo  
236 enriched region is free of nitriding, whereas Cr<sub>2</sub>N is detected below the Mo enriched zones [13]. This is  
237 strictly not the case for Cr-36.1Mo-3Si in the present investigation and assigned to the higher Mo  
238 content.

239 The SEM-EDS maps and a schematic mockup of the scales on Cr-36.1Mo-3Si after oxidation at 1100°C  
240 for 100 h are shown in Figure 3c and d. The continuous white lines in the elemental maps in Figure 3c  
241 mark the outer Corundum prototype Cr<sub>2</sub>O<sub>3</sub> (D5<sub>1</sub>, see Supplementary Material S2). Below the outer scale,  
242 a Cr depleted region is marked in the elemental maps of Cr and Mo. In the surface close region below  
243 the oxide layer, intra- and intergranular particles are identified with an increased Si and O concentration.  
244 It is assumed that SiO<sub>2</sub> is formed at these locations. An accurate determination of the stoichiometry of  
245 the oxide is, however, not reasonable considering the limited lateral resolution of SEM-EDS and the  
246 small size of the particles. The observation of SiO<sub>2</sub> formation agrees with results from Refs. [8,25,26]  
247 for the oxidation of Cr-Si alloys at 1200 and 1300°C, with the difference that the SiO<sub>2</sub> was limited to  
248 the grain boundaries. This can be either due to the lower oxidation temperature, where O diffusion is

249 limited to the grain boundaries. The Si enrichment at grain boundaries deeper in the substrate is due to  
250 the formation of  $(\text{Cr},\text{Mo})_3\text{Si}$  particles. 3 at.% Si are beyond the solubility limits at low temperatures,  
251 specifically for the Mo enriched interdendritic regions [26]. The thermal cycling from room temperature  
252 to 1100°C displays a sufficient heat treatment to form  $(\text{Cr},\text{Mo})_3\text{Si}$  under the presence of a nucleation site  
253 like the grain boundaries of the solid solution. Essential features of the schematic scale mockup in Figure  
254 3d are thus: (i) the layered  $\text{Cr}_2\text{O}_3$  scale, (ii) The Mo enriched layer just below the scale, (iii) the Si oxide  
255 layer at the interface as well as inter- and intragranular particles in the subsurface regions, and (vi)  
256  $(\text{Cr},\text{Mo})_3\text{Si}$  formed at the grain boundaries of the bulk material.

257 The scale exhibits a layered structure with a total scale thickness of 25  $\mu\text{m}$  after 100 h and Corundum  
258 prototype  $\text{Cr}_2\text{O}_3$  (D5<sub>1</sub>, see Supplementary Material S2) was identified as sole compound at the sample  
259 surface after 100 h via XRD. The scale growth occurs almost parabolic at  $(1.7 \pm 0.2) \cdot 10^{-11} \text{ cm}^2/\text{s}$  ( $R^2 \approx$   
260 0.92, see Supplementary Material S4) indicating diffusion control of the  $\text{Cr}_2\text{O}_3$  growth. This is similar  
261 to the reported rate constant for the silicide containing two-phase alloy Cr-32.2Mo-13.5Si at 1100 °C of  
262  $(1.1 \pm 0.3) \cdot 10^{-12} \text{ cm}^2/\text{s}$  ( $R^2 \approx 0.85$ ). In SEM-BSE micrographs, the scale adhesion at the interface  
263 between the substrate and the oxide scale appears intact and without buckling or cracks. However, the  
264 oxidation does not lead to a compact scale as illustrated in the mockup in Figure 3d but rather a complex  
265 layered outer  $\text{Cr}_2\text{O}_3$  scale in conjunction with some internal oxidation. The internal corrosion with Si  
266 oxide at the grain boundaries is observed in surface near regions. The progression of the depth of the  
267 internal oxidation follows a parabolic rate law at  $(8 \pm 1) \cdot 10^{-11} \text{ cm}^2/\text{s}$  ( $R^2 \approx 0.96$ , see Supplementary  
268 Material S4). Assuming that the internal oxidation is only caused by Si oxidizing to  $\text{SiO}_2$  and no  
269 oxidation of Cr or Mo occurs at the grain boundaries, the partial pressure of O can be estimated as the  
270 equilibrium of Si and  $\text{SiO}_2$  is met for a partial pressure of  $p_{\text{O}_2} \approx 10^{-19} \text{ Pa}$ , not taking the alloy activities  
271 into account [27]. The protective effect of Si enrichment at the interface and below in the substrate is  
272 due to the stability of  $\text{SiO}_2$  at lower oxygen partial pressures than Cr and especially Mo. Si dispersed at  
273 the interface forms  $\text{SiO}_2$  and acts as an O getter. The local O partial pressure decreases at the interface  
274 so that the underlying substrate does not oxidize. The positive effect of Si at the oxide/substrate interface  
275 on the oxidation of  $\text{Cr}_2\text{O}_3$  layers was also observed for the binary solid solution Cr-3Si compared to pure  
276 Cr in isothermal experiments at 1200°C [8]. Finally, the Mo enrichment seen in Figure 3d below the  
277 outer oxide scale successfully prevents nitridation [26].

278 In contrast to the scale on the Si free Cr-37.2Mo at 800°C, it is evident from the good scale adhesion,  
279 that  $\text{MoO}_3$  evaporation is successfully prevented in Cr-36.1Mo-3Si, which can be attributed to the  
280 formation of the discontinuous  $\text{SiO}_2$  layer within the scale and at the scale/substrate interface. The mass  
281 loss detected at 1100°C for Cr-36.1Mo-3Si is attributed to the evaporation of  $\text{CrO}_3$  from the surface of  
282 the oxide, but since the scale growth barely deviates from parabolic kinetics,  $\text{MoO}_3$  must also contribute  
283 here to some extent, e.g. when the scale develops flaws.

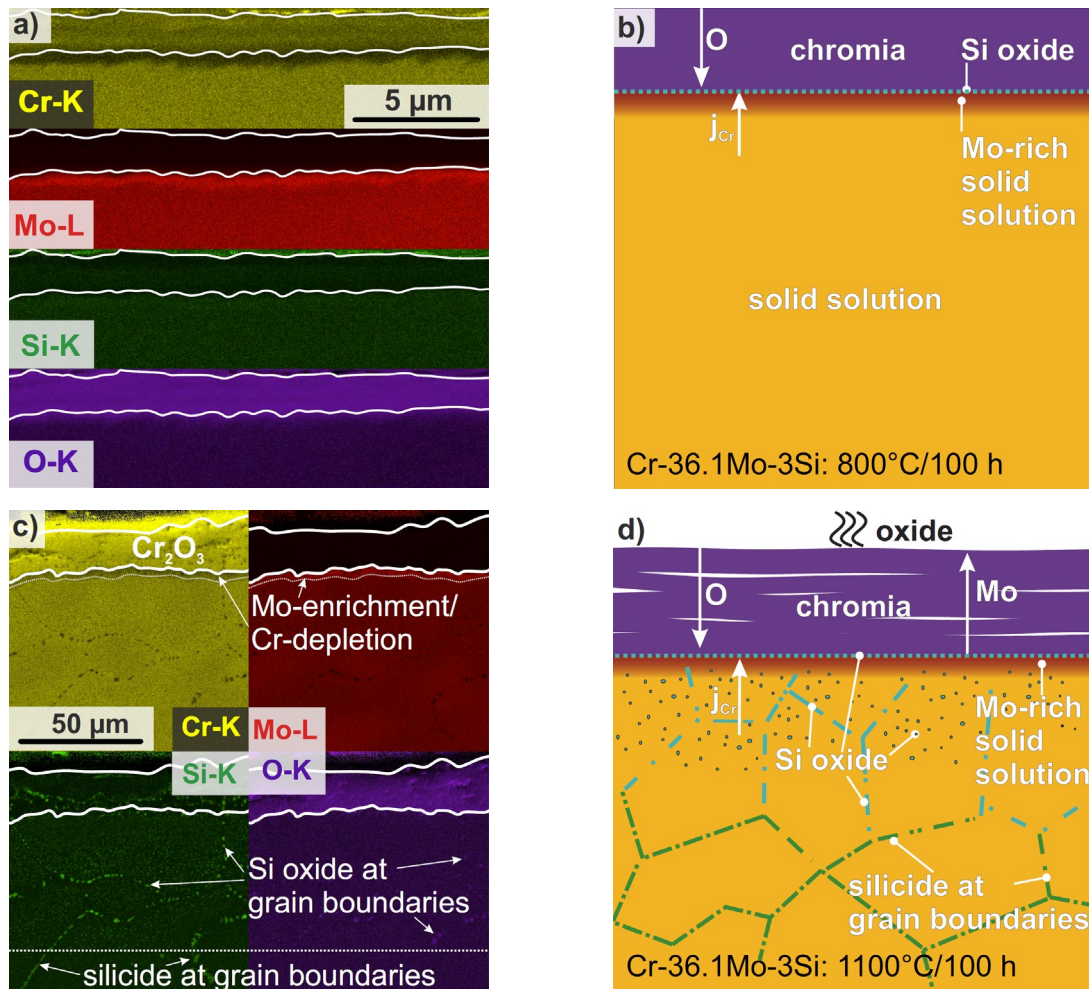


Figure 3: Oxide scale and microstructural changes close to the surface of Cr-36.1Mo-3Si after 100 h of oxidation at (a,b) 800°C and (c,d) 1100°C by (a,c) SEM-EDS and (b,d) as a schematic.

#### 4.2 Deformation Mechanisms

284 Figure 4a and b show orientation imaging microscopy maps obtained on longitudinal sections of  
 285 compression test samples deformed at room temperature and 900°C up to plastic strains of  
 286 approximately 6%. The color coded maps indicate the crystallographic orientation with respect to the  
 287 compression direction (vertical in the maps) and grayscale maps the diffraction pattern quality. Apart  
 288 from the qualitatively dominating blue and red grains in the color-coded maps, the quantitative  
 289 assessments of the crystallographic orientations in Figure 4c and d reveal  $\langle 100 \rangle / \langle 111 \rangle$  fiber texture  
 290 components along the compression axis. The maxima of the orientation distribution function are 1.6 to  
 291 1.9 multiples of the uniform distribution. In compression tests, the slip plane normal tends to rotate  
 292 toward the compression direction due to the confined strain release by dislocation slip. In bcc metals  
 293 and alloys with  $\langle 111 \rangle$  pencil glide of dislocations on  $\{1\bar{2}1\}$  to  $\{1\bar{3}2\}$  planes, this leads to mixed  
 294  $\langle 100 \rangle / \langle 111 \rangle$  fiber textures in compression [28]. Even when considering the low number of grains probed  
 295 in the present samples, the experimental observation is consistent with this expected trend.

296 Besides above confirmation of dislocation-mediated plasticity, deformation twinning is observed as  
 297 another deformation mechanism. In most grains, multiple twin systems are activated. All identified twin  
 298 systems without exception are of  $\{112\}\langle 11\bar{1} \rangle$  type (as confirmed by pole figure and trace analysis, see  
 299 Supplementary Material S5) and correspond to rotations of  $(60 \pm 2.9)^\circ$  about  $\langle 111 \rangle$  (misorientation  
 300 analysis) as the common twin system of bcc metals and alloys [29]. The number density of twin bands  
 301 is significantly lower at 900°C compared to room temperature as confirmed by the orientation maps

302 (only properly indexed twin bands were evaluated) as well as from the pattern quality maps (even  
303 showing unindexed twin bands as line features of low pattern quality terminating at grain boundaries).  
304 Furthermore, the twin lath thickness is larger at 900°C. The observation of twins coincides with the  
305 serrations observed in compression testing. In contrast to continuous deformation via dislocation slip,  
306 entire laths are discontinuously displaced during each twinning event, leading to stress drops. However,  
307 some short microcracks, located predominantly parallel to the compression direction, are also observed  
308 after deformation up to > 6% plastic strain. These cracks might originate from limited compatibility of  
309 large grains to transversal thickening. As cracking might also cause stress drops during testing,  
310 quantitative correlations, e.g. of twin number density and number or magnitude of stress drops cannot  
311 be made here.

312 Fundamentally, deformation twinning competes with dislocation slip as process for plastic deformation.  
313 Stresses required for twinning are usually larger as the ones for dislocation slip. Thus, the latter is the  
314 more commonly observed elementary process of initiation and continuation of plastic deformation in  
315 bcc metals and alloys (see e.g. [30] for a recent review of available literature). However, there are  
316 frequent reports also for deformation twinning in bcc refractory metals and alloys thereof, e.g. Mo  
317 [31,32], Cr [33], V [34], W [35], Nb [36,37], Ta [30], Cr-35Fe [33], Cr-Re solid solutions [33,38], Mo-  
318 35Re [39], and Nb-V solid solutions [21,40], both in polycrystalline [30,32–34,37–39,41] or single-  
319 crystalline condition [31,35,36,39]. Recently, twinning was also reported in a ternary, polycrystalline  
320 refractory metal alloy MoWRe even at deformation temperatures significantly exceeding those  
321 previously confirmed with deformation twinning [12]. As the two fundamental deformation mechanisms  
322 compete with each other depending on the internal stress level, a complex interdependency of intrinsic  
323 (solid solution, dislocation and grain boundary strengthening) and extrinsic parameters (temperature,  
324 strain rate) exists as is outlined in the following.

325 Available data for polycrystalline Mo [32], Cr [33], V [34] and Cr-15Re solid solutions [38] indicate a  
326 smaller twinning stress with increasing grain size. Consistently, the occurrence of twinning for the  
327 samples investigated here with a large grain size of > 100  $\mu\text{m}$  is more likely than for fine-grained  
328 samples. According to Ref. [42], the twinning stress in Cr is more sensitive to grain size as compared to  
329 dislocation slip, so that the onset stress of slip might surpass the twinning stress at large grain sizes.  
330 Thus, in these cases initiation of plastic deformation might be achieved by deformation twinning as  
331 opposed to dislocation slip. If the first stress drop is associated with the twinning stress [35–37], it is  
332 approximately equal for both alloys and varies between 350 and 500 MPa for all temperatures. It must  
333 be noted, however, that literature also reports counter examples, where deformation twinning occurred  
334 preferably at an intermediate grain size (Nb [37]), or where twinning stress increases with increasing  
335 grain size (Cr-35Re [38]).

336 Deformation twinning is often reported in bcc solid solutions, potentially due to increasing onset stress  
337 for dislocation mediated plasticity by solid solution strengthening (SSS) or by a reduced twinning stress  
338 due to alloying, the fundamental reasons of which remain unclear to date. Reid et al. [33] reported no  
339 twinning for Cr-4.9Re and Cr-15.2Re with similar grain sizes, but for Cr-35Re. Similarly, the same  
340 group of authors [39] reported deformation twinning in Mo-35Re, but not in Mo of similar grain size.  
341 This can be rationalized in the context of SSS as it increases the critical stress required for dislocation  
342 slip. For systems with large SSS, the dislocation slip might then again surpass the twinning stress. Owing  
343 to the large difference in lattice parameter and the large shear moduli for Mo and Cr, a beneficial  
344 influence of SSS on the activation of deformation twinning seems plausible [43]. Usually, deformation  
345 by twinning is assumed to be a low temperature and/or high strain rate process as in these cases the  
346 number of kink pairs formed (and thus, dislocation slip) are insufficient to accommodate plastic strain.

347 Weaver [41] suspected deformation twinning in Cr and Cr-IV at temperatures of 200-600°C, but did  
 348 not report microstructural or crystallographic proof. The aforementioned investigations on Nb-V and  
 349 MoWRe alloys also reported deformation twinning at elevated temperatures, up to 600°C in Nb-55V  
 350 [21] and 1000°C in MoWRe [44]. The alloys investigated here thus surpass the binary Nb-V solid  
 351 solutions and show twinning at absolute temperatures similarly high as compared to the ternary alloy  
 352 but at higher homologous temperature.

353 As deformation twins are high angle grain boundaries (and often incoherent due to elementary  
 354 dislocation processes during their formation), they impede dislocation motion. Deformation twinning  
 355 thus might contribute to a hierarchical grain boundary strengthening with increasing strengthening  
 356 contribution during plastic deformation similar to the observation in twinning induced plasticity (TWIP)  
 357 [45] or transformation induced plasticity (TRIP) steels. This might contribute to the high work hardening  
 358 obtained in this work, and displayed in Figure 2d.

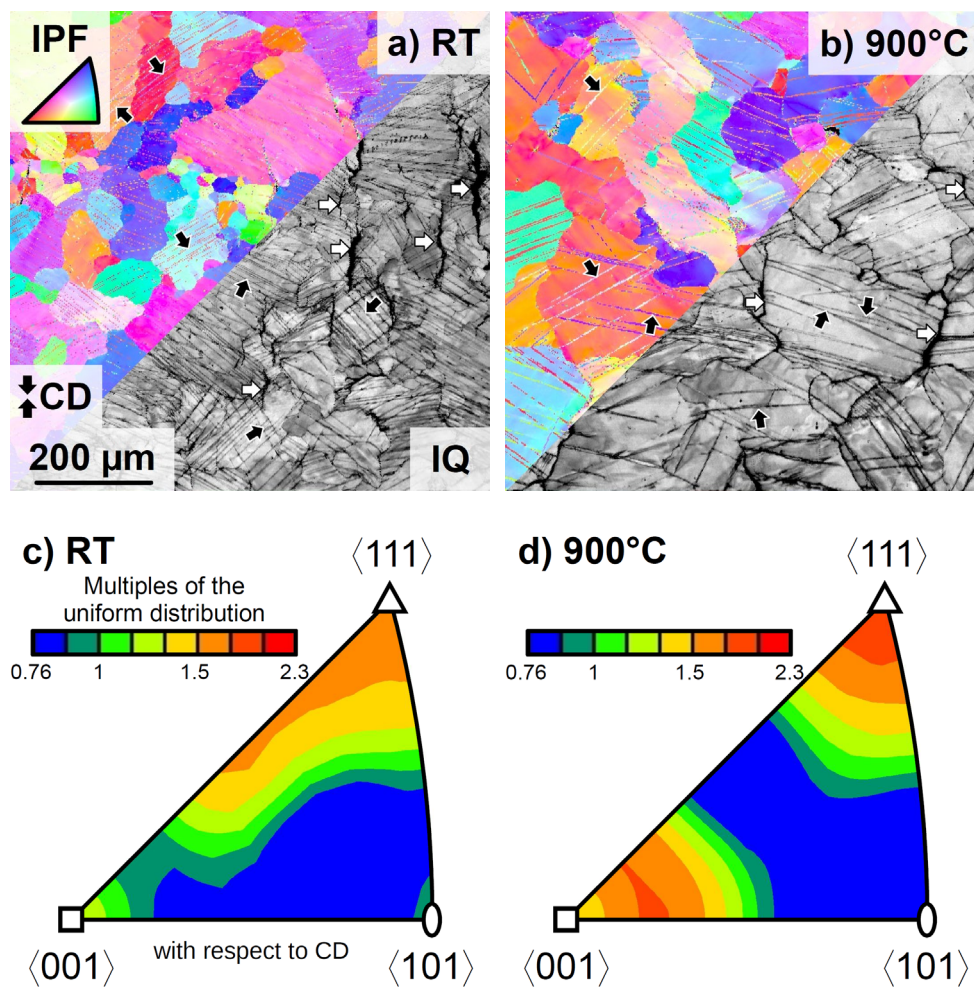


Figure 4: Microstructural changes induced by mechanical testing of Cr-36.1Mo-3Si in compression up to a plastic strain of approximately 6% at (a) room temperature and (b) 900°C. The color-code in the orientation maps (a,b) corresponds to the inverse pole figure of the compression direction (CD) in the in-set and grayscale image parts highlight diffraction pattern quality. Black arrows indicate deformation twins and white arrows longitudinal cracks along grain boundaries. (c,d) Orientation distribution function after the compression tests represented in the inverse pole figure of the CD as multiples of the uniform distribution.

## 5. Mechanisms to overcome fundamental barriers for the application of refractory metal-based alloys

359 The present materials development relies on the utilization of refractory metal elements that exhibit  
360 characteristic, intrinsic problems in oxidation limiting their application. Instead of tackling this by the  
361 formation of high amounts of brittle intermetallic phases that provide a reservoir of passivating elements,  
362 the choice of Cr and Mo individually addresses the intrinsic problems during oxidation: Cr leads to the  
363 formation of a protective Cr<sub>2</sub>O<sub>3</sub> scale while the Mo enrichment in the subsurface zone due to outward  
364 diffusion of Cr converts these regions to be resistant against nitridation. Si as a minor third element  
365 addition to the alloy guarantees the slow growth of the Cr<sub>2</sub>O<sub>3</sub> scale potentially by the additional  
366 formation of a SiO<sub>2</sub> subscale.

367 The low amount of Si needed in conjunction with the high temperature miscibility of Cr and Mo allows  
368 for the synthesis of single-phase, disordered solid solutions (the miscibility gap obtained for  
369 thermodynamic equilibrium does not lead to decomposition under relevant practical cooling  
370 conditions or only after cycling beyond the 100 h tested in this study [46]). Apart from this fundamental  
371 prerequisite to obtain ductility, the appearance of both dislocation slip and deformation twinning is  
372 confirmed, the latter of which might be facilitated by a high SSS contribution. The hierarchical  
373 refinement of the microstructure by deformation twinning during plastic deformation contributes to a  
374 very good work hardening behavior.

375 The materials presented here display the simplest manufacturing conditions possible with the relevant  
376 property profile being met. All further optimization treatments known from classical metallurgy might  
377 additionally be applied to the Cr-Mo-Si system to achieve improved and application relevant properties,  
378 such as microstructural stability, corrosion resistance as well as further strengthening, fatigue and creep  
379 resistance, e.g. by second phase particles.

### Acknowledgements

380 We gratefully acknowledge financial support by the Deutsche Forschungsgemeinschaft (DFG) within  
381 the framework of GRK 2561 MatCom-ComMat. We furthermore acknowledge the support from the  
382 Alexander von Humboldt Foundation for their cooperative research conducted under the Humboldt  
383 Fellowship of HI. This work was partly carried out with the support of the Karlsruhe Nano Micro Facility  
384 (KNMFi, [www.knmf.kit.edu](http://www.knmf.kit.edu)), a Helmholtz Research Infrastructure at Karlsruhe Institute of Technology  
385 (KIT, [www.kit.edu](http://www.kit.edu)). We acknowledge the chemical analysis by HCGE at the Institute for Applied  
386 Materials (IAM-AWP) by Dr. Bergfeldt, Karlsruhe Institute of Technology (KIT). We thank Bonita  
387 Beichert and Charlotte Wehnes for experimental support.

### Conflict of Interest

388 The authors declare no conflict of interest.

### Data Availability Statement

389 The data presented in this study are available in KITopen at <https://doi.org/10.35097/1866> under CC  
390 BY-SA 4.0 license. Further information is available upon request with [alexander.kauffmann@kit.edu](mailto:alexander.kauffmann@kit.edu).

## Materials and Methods

391 Alloys with the desired compositions of Cr-37.2Mo (at.%, throughout the document unless stated  
392 otherwise) and Cr-36.1Mo-3Si were manufactured from elemental Mo 99.95% (Plansee SE, Reutte,  
393 Austria), Cr 99+% (EVOChem, Offenbach am Rhein, Germany) and Si 99.99% (ChemPUR, Karlsruhe,  
394 Germany) in a standard arc melting process using an AM/0.5 arc melter (Edmund Bühler GmbH,  
395 Bodelshausen, Germany). Melting was performed in Ar (> 99.998 %) atmosphere in a water-cooled Cu  
396 crucible. The pressure during arc melting was 600 mbar. Before each remelting step, the melting of a  
397 piece of Zr was performed to bind residual O. The ingots were flipped and remelted five times to ensure  
398 homogeneity. The ingots were subsequently cut by electrical discharge machining into cuboidal samples  
399 of  $(5 \times 5 \times 4)$  mm<sup>3</sup> for oxidation experiments and  $(5 \times 3 \times 3)$  mm<sup>3</sup> for compression testing.

400 All surfaces of oxidation samples were ground with SiC paper of P2500 grit size. The surface area of  
401 the samples was obtained by optical macroscopy (Wild-Heerbrugg M420, Heerbrugg, Switzerland, and  
402 Olympus Stream Enterprise 1.7, Tokyo, Japan). Cyclic oxidation was performed at 800 and 1100°C in  
403 laboratory air using muffle furnaces (Carbolite Gero GmbH & Co. KG, Neuhausen, Germany). At least  
404 three samples were tested at each temperature. Average specific mass changes were determined from  
405 these samples and uncertainty was estimated using the standard deviation.

406 The duration of the oxidation cycles started with 1 h cycles for the first 20 h of oxidation. Afterwards,  
407 the cycle duration was increased to 5 h until total oxidation time was 50 h, followed by 10 h cycles until  
408 the samples have been exposed for 100 h in total. The oxidation samples were placed in Al<sub>2</sub>O<sub>3</sub> crucibles  
409 and weighed with the crucibles between oxidation intervals. Initial mass and mass changes of the  
410 oxidation samples were tracked after each oxidation cycle using a precision balance with an accuracy  
411 of 1 µg (Sartorius, Göttingen, Germany). Oxide scale thicknesses were determined manually by  
412 processing SEM-BSE micrographs of cross sections using the open source image processing software  
413 ImageJ (version 1.53c) after 1, 10 and 100 h of cyclic oxidation [47]. The oxide layer was examined  
414 with regard to its morphology on the substrate, the types of oxide grown and the element distribution  
415 within the oxide layer.

416 The  $(3 \times 3)$  mm<sup>2</sup> surfaces of the compression test samples were prepared by grinding with SiC paper of  
417 P2500 grit size using a self-constructed sample holder to ensure parallel contact faces. Dimensions of  
418 each specimen were measured using a digital indicator with 1 µm resolution (Sylvac SA, Yverdon-les-  
419 Bains, Switzerland). Compression tests were performed using a UPM-Zwick 1478 universal testing  
420 device (ZwickRoell, Ulm, Germany) with an induction coil to heat the samples to testing temperatures  
421 of up to 900°C. To minimize friction between the sample surfaces and punches, BN was applied to the  
422 sample surfaces. All tests, except from the ones at RT, were started after sufficient holding time of  
423 15 min at each test temperature to ensure the temperature being evenly distributed. The initial  
424 engineering strain rate was set to  $1 \cdot 10^{-4}$  s<sup>-1</sup>. Displacement was measured by a capacitive strain gauge  
425 attached to the Al<sub>2</sub>O<sub>3</sub> punches as well as an inductive strain gauge tracking the displacement of the cross-  
426 head. The signals from the two strain gauges were compared so that malfunctions or device specific  
427 measurement artefacts could be interpreted as such. Stress-strain data were corrected for the non-linear  
428 initial loading range using the maximum slope detected for the elastic deformation. As plastic  
429 deformation is serrated/discontinuous in the present case, stress at 1% plastic offset strain was evaluated  
430 for all samples. At each temperature, two samples of each composition were tested.

431 Samples for microstructural analysis in the as-cast and oxidized condition were cold mounted in  
432 VariKem 200 resin, ground to grit P2500 with SiC paper followed by 3 and 1 µm diamond polishing  
433 steps. Surface finish was achieved using a colloidal OP-S suspension (Buehler ITW, Leinfelden-

434 Echterdingen, Germany). SEM-BSE micrographs of the as-cast and the oxide scales were taken at 20 kV  
435 acceleration voltage on a LEO Gemini 1530 (Carl Zeiss AG, Oberkochen, Deutschland) scanning  
436 electron microscope (SEM).

437 Energy-dispersive X-ray spectroscopy (SEM-EDS) and electron backscatter diffraction (SEM-EBSD)  
438 were performed on an Auriga 60 (Carl Zeiss AG, Oberkochen, Deutschland) SEM equipped with an  
439 Octane Super EDS detector and an EDAX DigiView EBSD camera (Ametek, Berwyn, Pennsylvania,  
440 USA). For SEM-EDS analysis, the SEM was operated at 16 kV acceleration voltage. Standard-free,  
441 ZAF corrected SEM-EDS maps were created to visualize the element distributions in the oxide layers  
442 and close-to-surface substrate region. The K lines for Cr, Si and O and the L line for Mo were used to  
443 quantify the element distribution. For SEM-EBSD, the SEM was set to 20 kV acceleration voltage and  
444 a 120  $\mu\text{m}$  apertures was used. EDAX Team was used to acquire the EBSD maps using a W prototype  
445 phase for indexing. Overview maps are  $(840 \times 840) \mu\text{m}^2$  in size with a hexagonal grid of 2  $\mu\text{m}$  step size.  
446 Detailed maps of twinned regions were acquired with a size of  $(150 \times 150) \mu\text{m}^2$  at a step size of 500 nm.  
447 The indexing rate was about  $125 \text{ s}^{-1}$  with a successful indexing rate above 98%. The twin elements were  
448 identified using pole figures of the  $\{112\}$  habit plane with  $\langle 11\bar{1} \rangle$  shear direction and  $\{1\bar{1}0\}$  shear plane  
449 normal. The surface traces of the twin boundaries were considered in the analysis as well.

450 Crystal structures and lattice parameters were determined through X-ray diffraction (XRD). The  
451 diffraction patterns were recorded in Bragg-Brentano geometry with  $\theta/\theta$  focusing using a D2 phaser  
452 (Bruker Corp., Billerica, MA, USA) equipped with a LynxEye line detector. The X-ray tube with Cu-  
453  $K\alpha$  radiation was operated at 30 kV and 10 mA. Scans were performed between  $2\theta = 10^\circ - 145^\circ$ . The  
454 step size was  $0.01^\circ$  in  $2\theta$  with an accumulated acquisition time of 384 s per step. The sample was rotated  
455 to improve statistics. For phase identification, diffraction patterns were analyzed using the open source  
456 software PowderCell, version 2.4 [48]. The cubic lattice parameter of the W prototype crystal structures  
457 of the solid solutions were determined by extrapolating the measured lattice parameters towards  $\theta = 90^\circ$   
458 by using the weight function  $\frac{1}{2}(\cot^2 \theta + \cot \theta \cdot \cos \theta)$ , similar to the approach suggested by Nelson  
459 and Riley [49].

460 The Calphad software package Pandat (version 2023) with the proprietary database PanHEA  
461 (version 2023) was used to determine the solidus temperature for each alloy investigated here. For this,  
462 the calculations were performed for thermodynamic equilibrium by means of the PanEngine.

## Author Contributions

Frauke Hinrichs: Investigation, Formal analysis, Data Curation, Visualization, Project administration,  
Writing - Original Draft, Writing - Review & Editing

Georg Winkens: Formal analysis, Software, Writing - Original Draft, Writing - Review & Editing

Lena Kramer: Investigation, Formal analysis, Data Curation, Writing - Review & Editing

Daniel Schliephake: Formal analysis, Data Curation, Visualization, Writing - Original Draft, Writing -  
Review & Editing

Gabriely Falcão: Formal analysis, Writing - Review & Editing

Matthias Galetz: Supervision, Funding acquisition, Writing - Review & Editing

Haruyuki Inui: Funding acquisition, Writing - Review & Editing

Alexander Kauffmann: Investigation, Methodology, Formal analysis, Data Curation, Visualization, Supervision, Writing - Original Draft, Writing - Review & Editing

Martin Heilmaier: Supervision, Resources, Funding acquisition, Writing - Review & Editing

## References

- [1] A. Schwab, A. Thomas, J. Bennett, E. Robertson, S. Cary, *Electrification of Aircraft: Challenges, Barriers, and Potential Impacts*, (2021). <https://www.nrel.gov/docs/fy22osti/80220.pdf>. (accessed December 12, 2023).
- [2] J. Mukhopadhyaya, B. Graver, *Performance analysis of regional electric aircraft*, (2022). <https://theicct.org/publication/global-aviation-performance-analysis-regional-electric-aircraft-jul22/> (accessed December 12, 2023).
- [3] J.H. Perepezko, *The Hotter the Engine, the Better*, *Science*. 326 (2009) 1068–1069. <https://doi.org/10.1126/science.1179327>.
- [4] J.H. Perepezko, M. Krüger, M. Heilmaier, *Mo-Silicide Alloys for High-Temperature Structural Applications*, *Matls. Perf. Charact.* 10 (2021) 20200183. <https://doi.org/10.1520/MPC20200183>.
- [5] P. Tsakiroopoulos, *Alloys for application at ultra-high temperatures: Nb-silicide in situ composites*, *Progress in Materials Science*. 123 (2022) 100714. <https://doi.org/10.1016/j.pmatsci.2020.100714>.
- [6] O.N. Senkov, D.B. Miracle, K.J. Chaput, J.-P. Couzinie, *Development and exploration of refractory high entropy alloys—A review*, *J. Mater. Res.* 33 (2018) 3092–3128. <https://doi.org/10.1557/jmr.2018.153>.
- [7] E.S. Jones, Capt.J.F. Mosher, R. Speiser, J.W. Spretnak, *The Oxidation of Molybdenum*★, *Corrosion*. 14 (1958) 20–26. <https://doi.org/10.5006/0010-9312-14.1.20>.
- [8] A. Soleimani-Dorcheh, M.C. Galetz, *Oxidation and Nitridation Behavior of Cr–Si Alloys in Air at 1473 K*, *Oxid Met.* 84 (2015) 73–90. <https://doi.org/10.1007/s11085-015-9544-5>.
- [9] E.A. Gulbransen, K.F. Andrew, *A Preliminary Study of the Oxidation and Vapor Pressure of Chromium*, *J. Electrochem. Soc.* 99 (1952) 402. <https://doi.org/10.1149/1.2779609>.
- [10] D. Schliephake, A. Kauffmann, X. Cong, C. Gombola, M. Azim, B. Gorr, H.-J. Christ, M. Heilmaier, *Constitution, oxidation and creep of eutectic and eutectoid Mo-Si-Ti alloys*, *Intermetallics*. 104 (2019) 133–142. <https://doi.org/10.1016/j.intermet.2018.10.028>.
- [11] F. Hinrichs, A. Kauffmann, A.S. Tirunilai, D. Schliephake, B. Beichert, G. Winkens, K. Beck, A.S. Ulrich, M.C. Galetz, Z. Long, H. Thota, Y. Eggeler, A. Pundt, M. Heilmaier, *A novel nitridation- and pesting-resistant Cr-Si-Mo alloy*, *Corrosion Science*. 207 (2022) 110566. <https://doi.org/10.1016/j.corsci.2022.110566>.
- [12] O.N. Senkov, J.M. Scott, S.V. Senkova, D.B. Miracle, C.F. Woodward, *Microstructure and room temperature properties of a high-entropy TaNbHfZrTi alloy*, *Journal of Alloys and Compounds*. 509 (2011) 6043–6048. <https://doi.org/10.1016/j.jallcom.2011.02.171>.
- [13] A.S. Ulrich, P. Pfizenmaier, A. Solimani, U. Glatzel, M.C. Galetz, *Improving the oxidation resistance of Cr-Si-based alloys by ternary alloying*, *Corrosion Science*. 165 (2020) 108376. <https://doi.org/10.1016/j.corsci.2019.108376>.
- [14] E. Rudy, H. Nowotny, *Eine sigma-Phase im System Chrom-Molybdän-Silicium*, *Monatsh. Chem.* 105 (1974) 156–168.
- [15] D. Sturm, M. Heilmaier, J.H. Schneibel, P. Jéhanno, B. Skrotzki, H. Saage, *The influence of silicon on the strength and fracture toughness of molybdenum*, *Materials Science and Engineering: A*. 463 (2007) 107–114. <https://doi.org/10.1016/j.msea.2006.07.153>.
- [16] H.J. Goldschmidt, J.A. Brand, *The constitution of the chromium-niobium-silicon system*, *Journal of the Less Common Metals*. 3 (1961) 34–43. [https://doi.org/10.1016/0022-5088\(61\)90041-8](https://doi.org/10.1016/0022-5088(61)90041-8).
- [17] S. Obert, A. Kauffmann, S. Seils, S. Schellert, M. Weber, B. Gorr, H.-J. Christ, M. Heilmaier, *On the chemical and microstructural requirements for the pesting-resistance of Mo–Si–Ti alloys*, *Journal of Materials Research and Technology*. 9 (2020) 8556–8567. <https://doi.org/10.1016/j.jmrt.2020.06.002>.
- [18] V. Supatarawanich, D.R. Johnson, C.T. Liu, *Oxidation behavior of multiphase Mo–Si–B alloys*, *Intermetallics*. 12 (2004) 721–725. <https://doi.org/10.1016/j.intermet.2004.02.011>.
- [19] R. Mitra, *Mechanical behaviour and oxidation resistance of structural silicides*, *International Materials Reviews*. 51 (2006) 13–64. <https://doi.org/10.1179/174328006X79454>.
- [20] A.S. Dorcheh, M.C. Galetz, *Challenges in Developing Oxidation-Resistant Chromium-Based Alloys for Applications Above 900°C*, *JOM*. 68 (2016) 2793–2802. <https://doi.org/10.1007/s11837-016-2079-7>.

- [21] T. Shimomura, T. Kainuma, R. Watanabe, Mechanical properties of vanadium-niobium alloys, *Journal of the Less Common Metals*. 57 (1978) 147–159. [https://doi.org/10.1016/0022-5088\(78\)90235-7](https://doi.org/10.1016/0022-5088(78)90235-7).
- [22] I.S. Yasnikov, A. Vinogradov, Y. Estrin, Revisiting the Considère criterion from the viewpoint of dislocation theory fundamentals, *Scripta Materialia*. 76 (2014) 37–40. <https://doi.org/10.1016/j.scriptamat.2013.12.009>.
- [23] E.A. Gulbransen, K.F. Andrew, Kinetics of the Oxidation of Chromium, *J. Electrochem. Soc.* 104 (1957) 334. <https://doi.org/10.1149/1.2428576>.
- [24] S.V. Raj, An evaluation of the properties of Cr<sub>3</sub>Si alloyed with Mo, *Materials Science and Engineering: A*. 201 (1995) 229–241. [https://doi.org/10.1016/0921-5093\(95\)09767-8](https://doi.org/10.1016/0921-5093(95)09767-8).
- [25] L. Royer, X. Ledoux, S. Mathieu, P. Steinmetz, On the Oxidation and Nitridation of Chromium at 1300 °C, *Oxid Met.* 74 (2010) 79–92. <https://doi.org/10.1007/s11085-010-9198-2>.
- [26] L. Koliotassis, E.M.H. White, M.C. Galetz, The influence of Mo-content and annealing on the oxidation behavior of arc-melted Cr-xMo-8Si-alloys (Mo = 10-40at.%), *Advanced Engineering Materials*. (2023).
- [27] H.J.T. Ellingham, Reducibility of oxides and sulphides in metallurgical processes, *J. Soc. Chem. Ind.* (1944) 125–133.
- [28] U.F. Kocks, C.N. Tomé, H.-R. Wenk, *Texture and anisotropy: preferred orientations in polycrystals and their effect on materials properties*, Cambridge University Press, Cambridge, 2005.
- [29] F.R.N. Nabarro, M.S. Duesbery, eds., *Dislocations in solids*, North-Holland Pub. Co, Amsterdam ; New York, 1979.
- [30] C.Q. Chen, J.N. Florando, M. Kumar, K.T. Ramesh, K.J. Hemker, Incipient deformation twinning in dynamically sheared bcc tantalum, *Acta Materialia*. 69 (2014) 114–125. <https://doi.org/10.1016/j.actamat.2014.01.046>.
- [31] F. Guiu, P.L. Pratt, The Effect of Orientation on the Yielding and Flow of Molybdenum Single Crystals, *Physica Status Solidi (b)*. 15 (1966) 539–552. <https://doi.org/10.1002/pssb.19660150214>.
- [32] B.J. Shaw, Twinning and the low temperature mechanical properties of polycrystalline niobium and molybdenum, *Journal of the Less Common Metals*. 13 (1967) 294–306. [https://doi.org/10.1016/0022-5088\(67\)90138-5](https://doi.org/10.1016/0022-5088(67)90138-5).
- [33] C.N. Reid, A. Gilbert, Dislocation structure in chromium, chromium-rhenium, and chromium-iron alloys, *Journal of the Less Common Metals*. 10 (1966) 77–90. [https://doi.org/10.1016/0022-5088\(66\)90116-0](https://doi.org/10.1016/0022-5088(66)90116-0).
- [34] T.G. Lindley, R.E. Smallman, The plastic deformation of polycrystalline vanadium at low temperatures, *Acta Metallurgica*. 11 (1963) 361–371. [https://doi.org/10.1016/0001-6160\(63\)90161-5](https://doi.org/10.1016/0001-6160(63)90161-5).
- [35] R.C. Koo, Effect of purity on the tensile properties of tungsten single crystals from –196°C to 29°C, *Acta Metallurgica*. 11 (1963) 1083–1095. [https://doi.org/10.1016/0001-6160\(63\)90197-4](https://doi.org/10.1016/0001-6160(63)90197-4).
- [36] N.A. Boucher, J.W. Christian, The influence of pre-strain on deformation twinning in niobium single crystals, *Acta Metallurgica*. 20 (1972) 581–591. [https://doi.org/10.1016/0001-6160\(72\)90013-2](https://doi.org/10.1016/0001-6160(72)90013-2).
- [37] K. Farrell, P.R.V. Evans, Some observations on mechanical twinning in polycrystalline niobium, *Journal of the Less Common Metals*. 8 (1965) 222–234. [https://doi.org/10.1016/0022-5088\(65\)90107-4](https://doi.org/10.1016/0022-5088(65)90107-4).
- [38] A.R. Rosenfield, Deformation twinning of polycrystalline chromium-rhenium alloys, *Journal of the Less Common Metals*. 7 (1964) 235–238. [https://doi.org/10.1016/0022-5088\(64\)90072-4](https://doi.org/10.1016/0022-5088(64)90072-4).
- [39] C.N. Reid, A. Gilbert, G.T. Hahn, *Investigation of the Relationship of Twinning to Brittle Fracture of Refractory Metals*, Directorate of Materials and Processes, Aeronautical Systems Division, Air Force Systems, 1963.
- [40] D.O. Holsen, *Deformation Twinning in the Columbium-vanadium Alloy System*, Oak Ridge National Laboratory, 1964.
- [41] C.W. Weaver, ‘Twinning’ and Fracture in Chromium, *Nature*. 193 (1962) 265–266. <https://doi.org/10.1038/193265a0>.
- [42] M.J. Marcinkowski, H.A. Lipsitt, The plastic deformation of chromium at low temperatures, *Acta Metallurgica*. 10 (1962) 95–111. [https://doi.org/10.1016/0001-6160\(62\)90055-X](https://doi.org/10.1016/0001-6160(62)90055-X).

- [43] F. Maresca, W.A. Curtin, Mechanistic origin of high strength in refractory BCC high entropy alloys up to 1900K, *Acta Materialia*. 182 (2020) 235–249. <https://doi.org/10.1016/j.actamat.2019.10.015>.
- [44] O.N. Senkov, S.I. Rao, G.H. Balbus, R. Wheeler, E.J. Payton, Microstructure and deformation behavior of MoReW in the temperature range from 25°C to 1500°C, *Materialia*. 27 (2023) 101688. <https://doi.org/10.1016/j.mtla.2023.101688>.
- [45] I. Gutierrez-Urrutia, D. Raabe, Dislocation and twin substructure evolution during strain hardening of an Fe–22wt.% Mn–0.6wt.% C TWIP steel observed by electron channeling contrast imaging, *Acta Materialia*. 59 (2011) 6449–6462. <https://doi.org/10.1016/j.actamat.2011.07.009>.
- [46] O. Kubaschewski, I. Barin, Phase equilibria in condensed systems, *Pure and Applied Chemistry*. 38 (1974) 469–494. <https://doi.org/10.1351/pac197438040469>.
- [47] C.A. Schneider, W.S. Rasband, K.W. Eliceiri, NIH Image to ImageJ: 25 years of image analysis, *Nat Methods*. 9 (2012) 671–675. <https://doi.org/10.1038/nmeth.2089>.
- [48] W. Kraus, G. Nolze, Powder Cell – a program for the representation and manipulation of crystal structures and calculation of the resulting X-ray powder patterns, *J Appl Crystallogr*. 29 (1996) 301–303. <https://doi.org/10.1107/S0021889895014920>.
- [49] J.B. Nelson, D.P. Riley, An experimental investigation of extrapolation methods in the derivation of accurate unit-cell dimensions of crystals, *Proc. Phys. Soc.* 57 (1945) 160–177. <https://doi.org/10.1088/0959-5309/57/3/302>.



# Supplementary Material to “Overcoming barriers for high temperature alloys: oxidation and ductility”

Frauke Hinrichs<sup>a</sup>, Georg Winkens<sup>a</sup>, Lena Katharina Kramer<sup>a</sup>, Daniel Schliephake<sup>a</sup>, Gabriely Falcão<sup>a</sup>, Mathias Christian Galetz<sup>b</sup>, Haruyuki Inui<sup>c,d</sup>, Alexander Kauffmann<sup>a,e,\*</sup> and Martin Heilmaier<sup>a</sup>

<sup>a</sup> Institute for Applied Materials (IAM-WK), Karlsruhe Institute of Technology (KIT), Engelbert-Arnold-Str. 4, 76131 Karlsruhe, Germany

<sup>b</sup> DECHEMA-Forschungsinstitut, High Temperature Materials, Theodor-Heuss-Allee 25, 60486 Frankfurt am Main, Germany

<sup>c</sup> Department of Materials Science and Engineering, Kyoto University, Sakyo-ku, Kyoto 606-8501, Japan

<sup>d</sup> Center for Elements Strategy Initiative for Structural Materials (ESISM), Kyoto University, Sakyo-ku, Kyoto 606-8501, Japan

<sup>e</sup> Karlsruhe Nano Micro Facility (KNMFi), Karlsruhe Institute of Technology (KIT), Hermann-von-Helmholtz-Platz 1, 76344 Eggenstein-Leopoldshafen, Germany

\* corresponding author

mail: alexander.kauffmann@kit.edu (A. Kauffmann)

phone: +49 721 608 42346

## 1. Crystal Structure

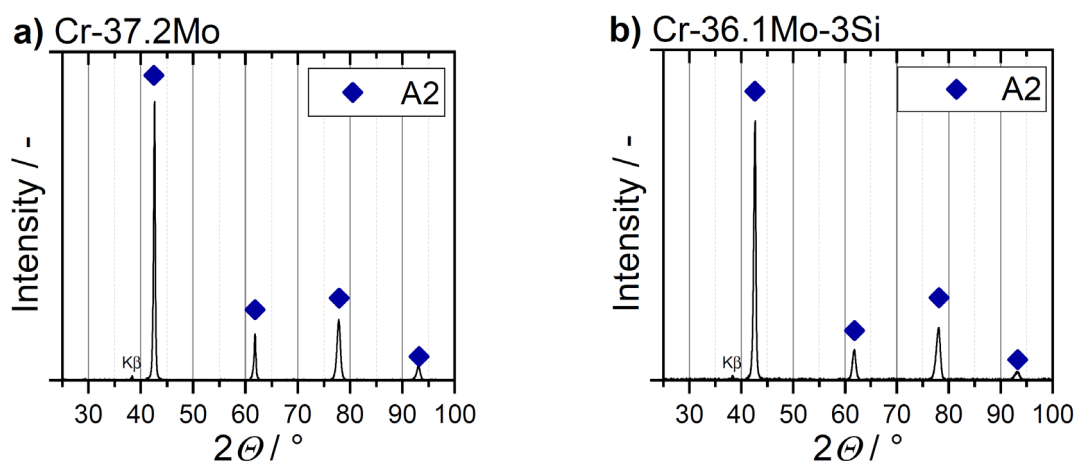


Figure S1: Confirmation of the A2 crystal structure in the testing condition by XRD (powder) of as cast: (a) Cr-37.2Mo and (b) Cr-36.1-3Si. A2 is the Strukturbericht designation of disordered body centered cubic *W* prototype.

## 2. Oxide Scales

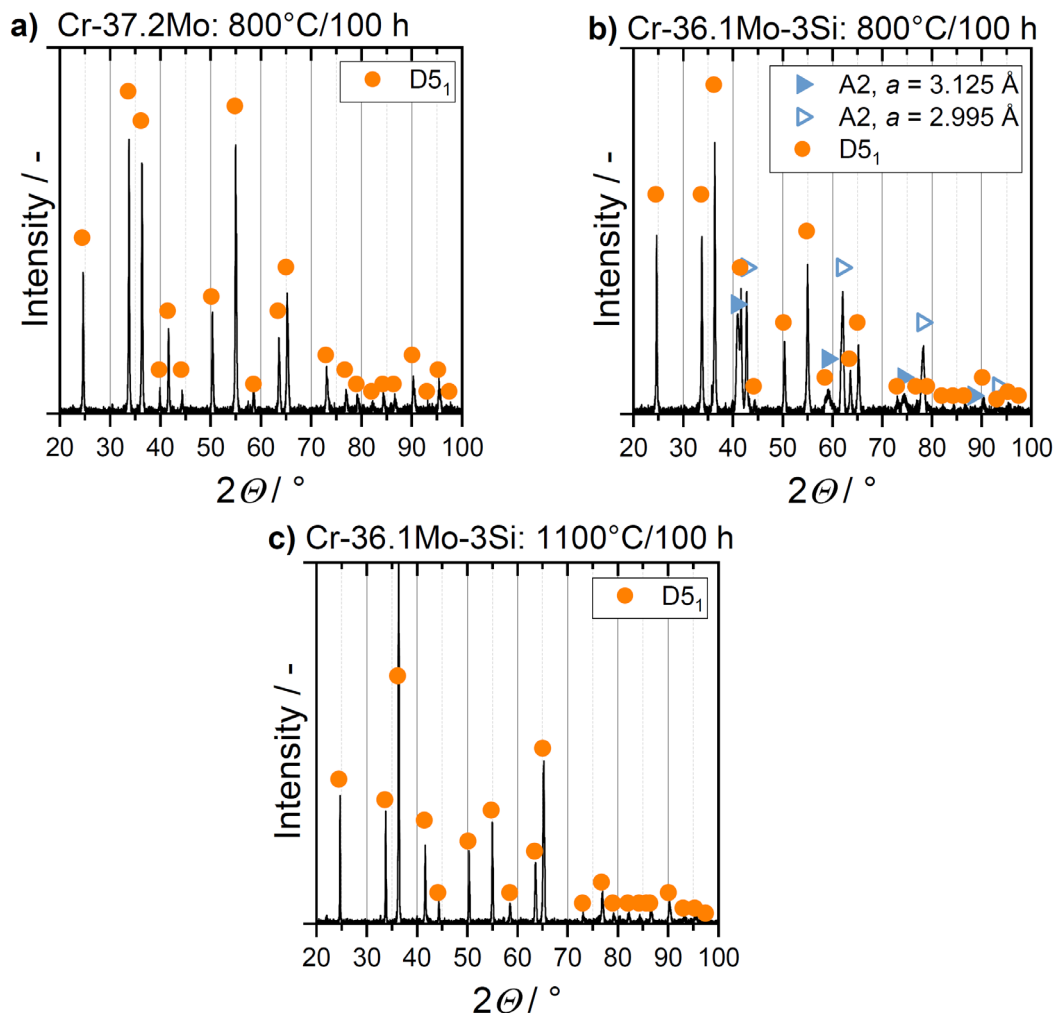


Figure S2: Confirmation of the  $D5_1$  crystal structure (Corundum prototype) of the oxide scales formed during 100 h of cyclic oxidation: a) Cr-37.2Mo at 800 °C, b) Cr-36.1Mo-3Si at 800 °C and c) Cr-36.1Mo-3Si at 1100 °C.

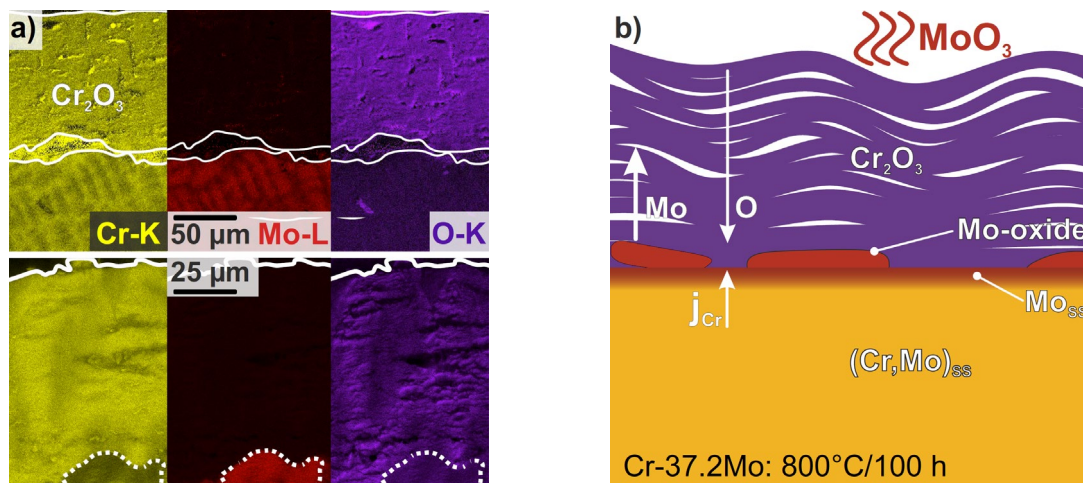


Figure S3: Mockup of the oxide scale and near-surface region of Cr-37.2Mo after 100 h of oxidation at 800°C: a) SEM-EDS and schematic.

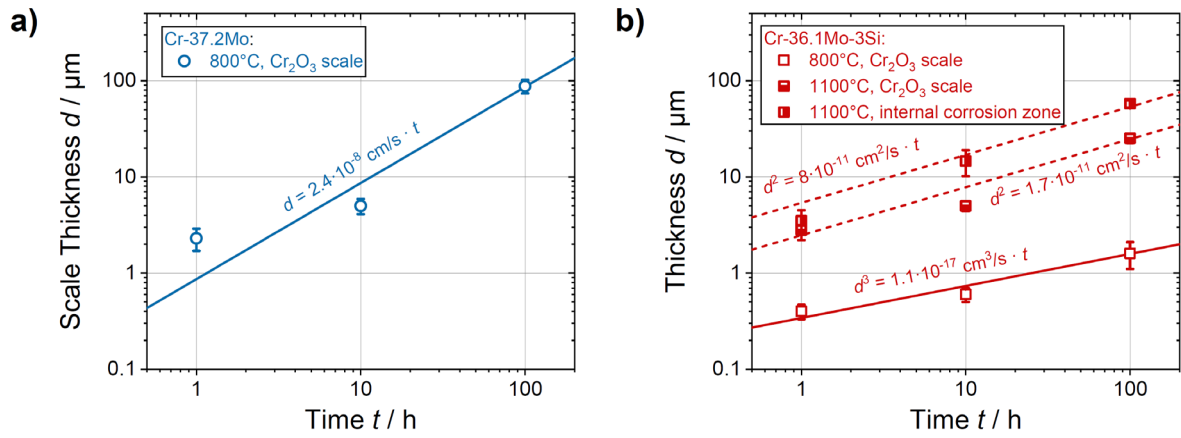
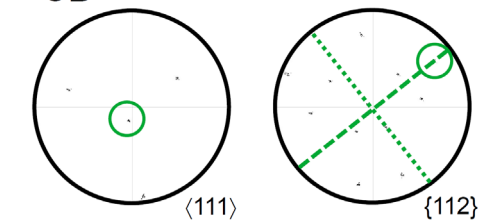
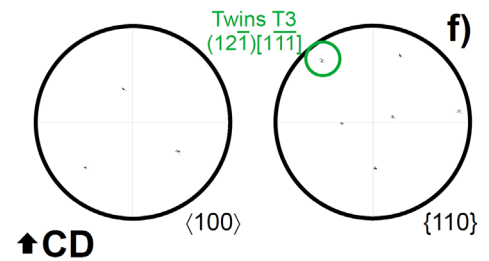
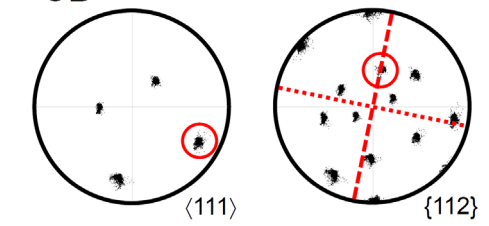
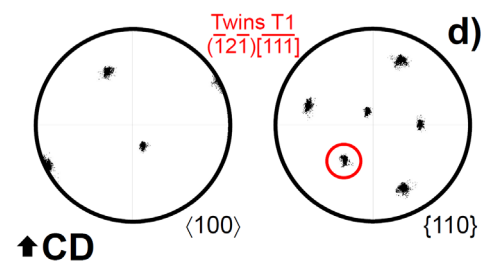
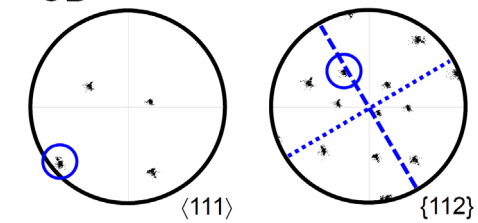
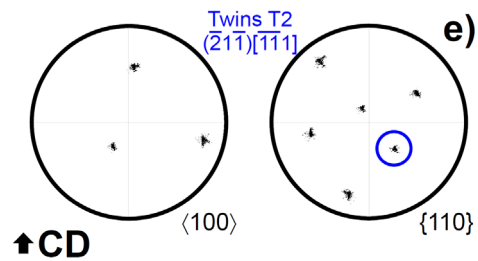
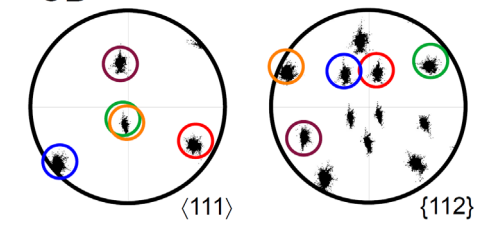
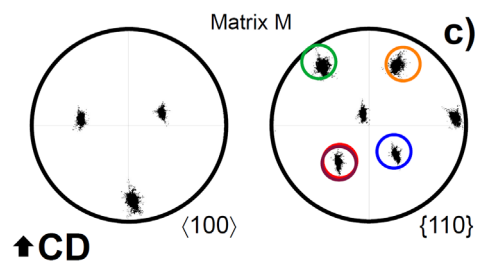
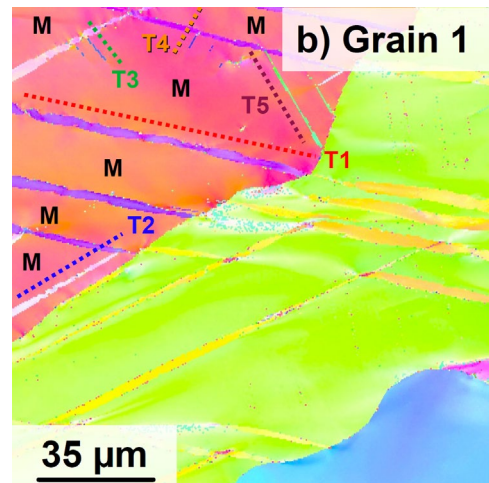
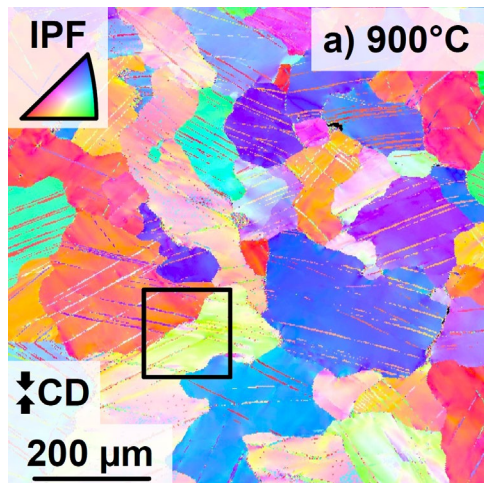


Figure S4: Oxide scale thicknesses as a function of oxidation time as determined from SEM-BSE micrograph image analyses: a) Cr-37.2Mo and b) Cr-36.1Mo-3Si. The fit lines represent fits of  $d^n = k_{n,d} \cdot t$  with  $n = 1, 2$  or  $3$  to the data.  $n$  is estimated from free fits and rounded.

### 3. Deformation Twinning



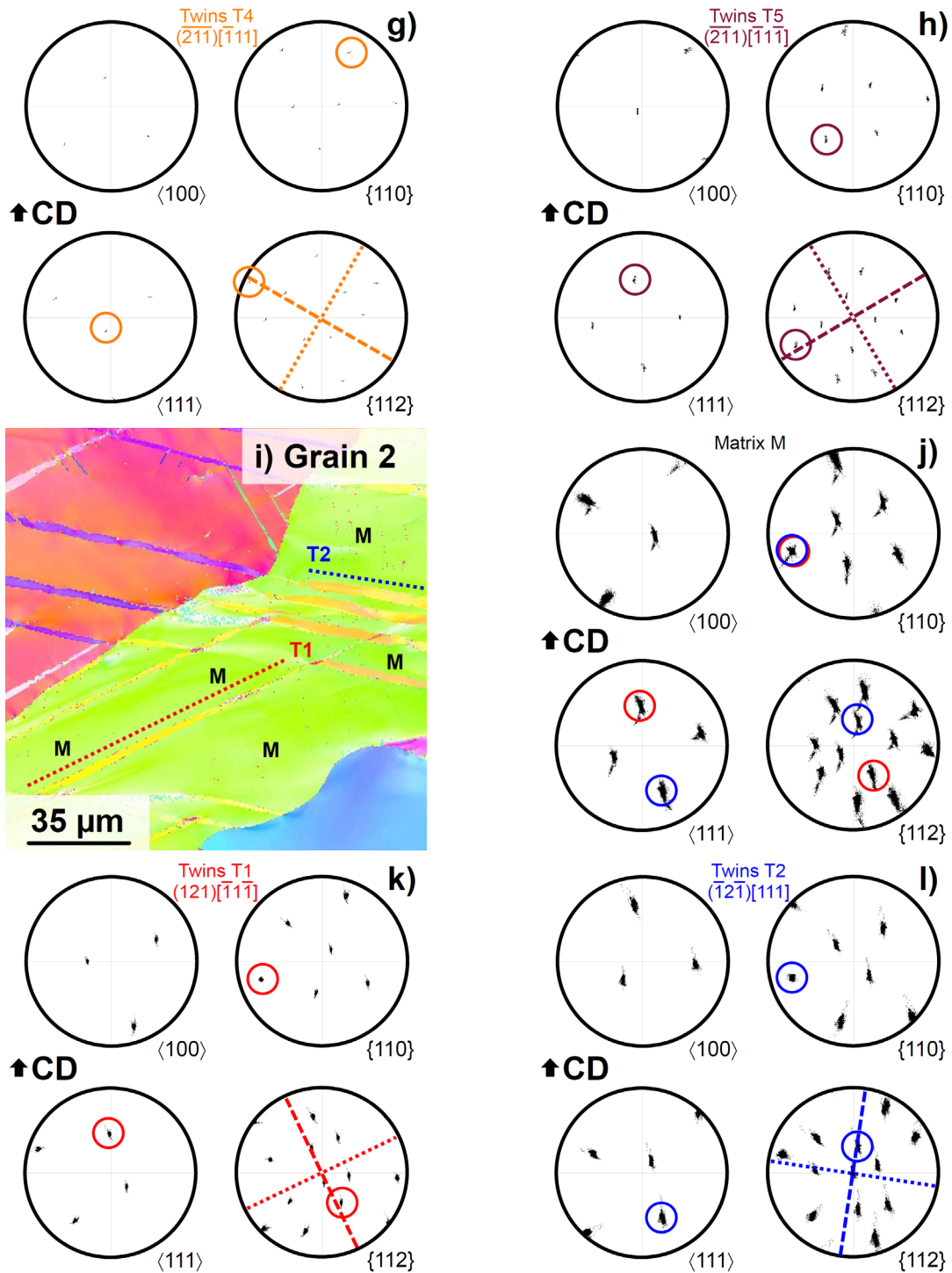


Figure S5: Analysis of the active twin systems after compression testing at 900°C up to a plastic strain of approximately 6% using SEM-EBSD: a) overview orientation map and (b,i) detail orientation map with indicated grains and twin lamellae. The color code corresponds to the inverse pole figure of the compression direction (CD) in a). The traces of the twin lamellae in the cross section are depicted as dotted lines and labelled with T1 to T5 whereas matrix grain regions are labelled with M. (c-h,j-l) Pole figures of characteristic elements for the matrix of the grains (M) and of the twins detected (T1 to T5) proving the exclusive activation of  $\{112\}\langle 11\bar{1}\rangle$  twin systems with  $\{1\bar{1}0\}$  shear planes. In the pole figures the lamella traces are again indicated as dotted lines and the potential pole directions of the twin plane normal as dashed lines. In all cases, the common  $\{112\}$  pole of the matrix and the respective twin always coincide with the potential plane normal orientations. Furthermore, the poles of the identified  $\langle 11\bar{1}\rangle$  and  $\{1\bar{1}0\}$ , also common to both matrix and twin, are always perpendicular to the identified  $\{112\}$  pole. The common poles are highlighted by color coded circles. Deviations from ideal sites are due to crystal reorientation by dislocation slip and, thus, depend on the strain of activation for a given twin system.